Chapter in **Advancing Astrophysics with the SKA – II**

Fast Radio Bursts as Cosmological Probes

Manisha Caleb,[1] Jéferson A. S. Fortunato,[2,3] Steffen Hagstotz,[4,5] Clancy W. James,[6] Joscha N. Jahns-Schindler,[7,8] Dylan Jow,[9] Evan Keane,[10] Koustav Konar,[11] Yin-Zhe Ma,[11] Daniele Michilli,[12] Robert Reischke*,[13] Amit Seta,[14] Priyanka Singh*,[15] Laura G. Spitler*,[16] Yidan Wang,[17] Amanda Weltman[2,3] and The SKA Transients SWG

[1]*Sydney Institute for Astronomy, School of Physics, The University of Sydney, Sydney, NSW 2006, Australia*
[2]*High Energy Physics, Cosmology & Astrophysics Theory (HEPCAT) Group, Department of Mathematics and Applied Mathematics, University of Cape Town, Cape Town, 7700, South Africa*
[3]*African Institute for Mathematical Sciences, 6 Melrose Road, Muizenberg, Cape Town, 7945, South Africa*
[4]*Universitäts-Sternwarte, Fakultät für Physik, Ludwig-Maximilians Universität München, Scheinerstraße 1, D-81679 München, Germany and*
[5]*Excellence Cluster ORIGINS, Boltzmannstraße 2, D-85748 Garching, Germany*
[6]*International Centre for Radio Astronomy Research, Curtin University, Bentley, 6102, WA, Australia*
[7]*Centre for Astrophysics and Supercomputing, Swinburne University of Technology, Hawthorn, VIC 3122, Australia*
[8]*ARC Centre of Excellence for Gravitational Wave Discovery (OzGrav), Hawthorn, VIC 3122, Australia*
[9]*Kavli Institute for Particle Astrophysics and Cosmology, Stanford University, 452 Lomita Mall, Stanford, CA 94305, USA*
[10]*School of Physics, Trinity College Dublin, College Green, Dublin 2, D02 PN40, Ireland*
[11]*Department of Physics, Stellenbosch University, Matieland 7602, South Africa*
[12]*Laboratoire d'Astrophysique de Marseille, Aix-Marseille University, CNRS, CNES, Marseille, France*
[13]*Argelander-Institut für Astronomie, Universität Bonn, Auf dem Hügel 71, D-53121 Bonn, Germany*
[14]*Research School of Astronomy and Astrophysics, Australian National University, Canberra, ACT 2611, Australia*
[15]*Department of Astronomy, Astrophysics and Space Engineering, Indian Institute of Technology, Indore 453552, India*
[16]*Max-Planck-Institut für Radioastronomie, Auf dem Hügel 69, 53121 Bonn, Germany*
[17]*National Astronomical Observatories, Chinese Academy of Sciences, Beijing 100101, China University of Chinese Academy of Sciences, Beijing 100049, China*
**Coordinating author*

E-mail: reischke@posteo.net, lspitler@mpifr-bonn.mpg.de

Fast radio bursts (FRBs) are brief, coherent radio pulses of extragalactic origin. They typically last from microseconds to milliseconds and have energies large enough to be visible over cosmological distances. Since FRBs interact with free electrons along their paths, the original burst is dispersed (Dispersion Measure, DM) and broadened (scattering). Furthermore, the burst's polarization is altered by Faraday rotation. Consequently, FRBs are excellent probes of the cosmological distribution of baryons, the expansion of the Universe, magnetic fields, and minuscule effects of fundamental physics that accumulate over vast distances.
This chapter is the second of a trilogy of FRB chapters and discusses FRBs as a standalone probe. We first introduce the foundation of FRB observables related to those questions. Next, we lay the groundwork for forecasting SKA's potential by describing the method to simulate the expected FRB population observable with the SKA. These synthetic FRB catalogues are then used to investigate the SKA's potential to probe the Universe's expansion rate and fundamental physics, such as the equivalence principle and the existence of massive photons. Furthermore, we investigate the possibility of tracing cosmic magnetic fields and investigating different dark matter candidates.

1 Introduction

Fast Radio Bursts (FRBs) are the first extragalactic radio sources with temporal variation on ~ms timescales (see Petroff et al., 2019, for a review), and due to their large luminosities, can be detected out to distances of many Gpc (Caleb et al., 2025). The physical properties of the ionized media along the FRB's path are encoded in the radio signal through several propagation effects, most prominently dispersion. They are also abundant, with $> 10^5$ occurring over the sky per day (e.g. Niu et al., 2021). Therefore, FRBs are a unique probe of the Universe.

The search for new FRBs with SKA is well suited for commensal observations with other surveys. Most cosmological applications benefit from a large number of sightlines, but their exact locations on the sky is generally not important. One exception is FRBs that travel through the Galactic plane may be of lower value for cosmology, because the Galaxy makes optical follow-up of the host galaxy difficult and imposes additional dispersion that can have high uncertainty, but provides a new probe of the Milky Way interstellar medium. In summary, an FRB search should be running whenever and wherever SKA is observing in order to detect as many FRBs over as much of the sky as possible.

Compared to other big telescopes in the FRB game, SKA excels in sensitivity and frequency coverage. Current telescopes that lead the blind search for FRBs are ASKAP (Hotan et al., 2021; Shannon et al., 2024), CHIME (CHIME/FRB Collaboration et al., 2021a; CHIME Collaboration et al., 2022), DSA-110[1] (Law et al., 2023), and MeerKAT (e.g. Rajwade et al., 2022; Caleb et al., 2023; Caleb et al., 2025). SKA-Mid will have higher sensitivity than these telescopes, but a lower instantaneous field of view in some cases. As a result, the expected detection rate is comparable to CHIME's current rate, although the FRB population observed by SKA will have a higher average redshift. FRBs at high redshifts are of particular interest, as we will discuss further below, and SKA, with its high sensitivity, will discover many of them.

In this chapter we provide the necessary background information for the use of FRBs as cosmological probes and describe a simulated sample of FRBs that could be detected by SKA-mid bands 1 and 2 and SKA-low for the AA* and AA4 configurations, based on our current knowledge of the population. These simulations are used as input for quantitative forecasts of several cosmological applications of FRBs. In this chapter we focus on the science of extragalactic magnetic fields (4), the expansion of the Universe (5), dark matter searches (6), and fundamental physics (7). A companion chapter focuses on using FRBs to study the distribution of baryonic matter in the Universe (Caleb et al., 2026). In addition, a separate chapter describes the potential of SKA for understanding the central engine(s) of FRBs (Curtin et al., 2026).

2 FRB Observables

In this section, we describe the fundamental observables that are used to analyse the medium traversed by FRBs. We will go into more detail about the different contributions in the relevant sections in this chapter, as well as in the FRBs as baryon tracers chapter (Caleb et al., 2026).

[1]The telescope names are acronyms standing, respectively, for Australian SKA Pathfinder, Canadian Hydrogen Intensity Mapping Experiment, and Deep Synoptic Array

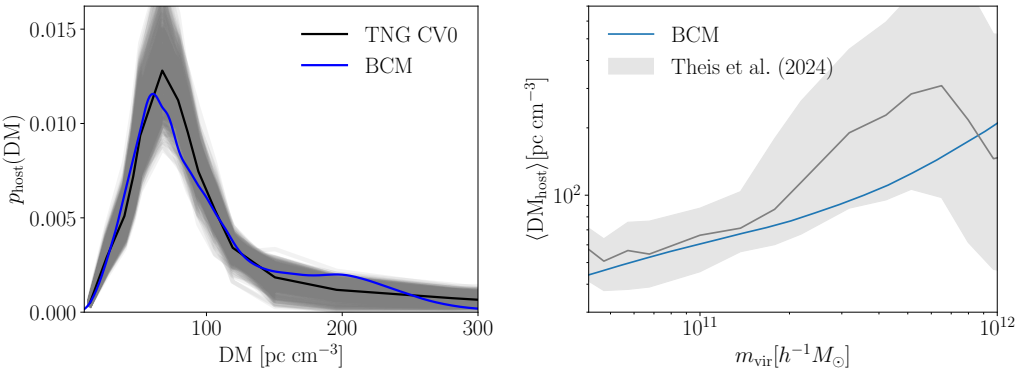

Figure 1: *Left*: Typical distributions of the host contribution as measured in the TNG simulation by Theis et al. (2024) with the model prediction from Reischke et al. (2025). *Right*: dependence of the host contribution on halo mass.

2.1 The dispersion measure

The dominating effect in FRB observations is the dispersion measure (DM). The arrival time of the photons at frequency ν is an integral over the inverse of the burst's group velocity. Using the dispersion relation of electromagnetic waves propagating through a cold plasma and expanding the inverse group velocity in terms of plasma frequency, one finds that the time delay is $\Delta t \propto \nu^{-2}$ and one defines the proportionality constant to be the DM

$$\mathrm{DM} = \int_0^{d_{\rm FRB}} n_{\rm e}(s)\,\mathrm{d}s\ , \tag{1}$$

where $d_{\rm FRB}$ is the distance to the FRB, $n_{\rm e}(s)$ is the free electron density, and the integral is carried out along the line-of-sight. Observationally, the DM of an FRB at redshift z (inferred from $d_{\rm FRB}$ or vice versa) and (two-dimensional) sky position $\boldsymbol{x}$ consists of different contributions from the distinct environments encountered by the burst:

$$\mathrm{DM_{obs}}(\mathbf{x}, z) = \mathrm{DM_{host}}(z) + \mathrm{DM_{cosmic}}(\mathbf{x}, z) + \mathrm{DM_{MW}}(\mathbf{x}) + \mathrm{DM_{MW,halo}}(\mathbf{x})\ . \tag{2}$$

$\mathrm{DM_{host}}$ is the host contribution originating from the burst's host galaxy as well as from its local environment. $\mathrm{DM_{cosmic}}$ describes the contribution from the mean free electron density and the large-scale structure (LSS) in the Universe. Lastly, $\mathrm{DM_{MW}}(\mathbf{x})$ and $\mathrm{DM_{MW,halo}}(\mathbf{x})$ are the contributions from the Milky Way and its halo. Hence, analysing the observed DM requires modelling each component. However, as indicated in Eq. (2), observing FRBs along different sightlines and at different redshifts can statistically distinguish the contributions. The following provides a short summary of the different contributions. A more detailed discussion will be provided in the corresponding sections.

2.1.1 The host contribution

The host contribution appears to be drawn from a highly skewed distribution with a long tail to large DM as a result of FRBs going off in the trailing edge of their respective host galaxy. This is also supported by analytical arguments (McQuinn, 2014; Reischke et al., 2025) and directly from

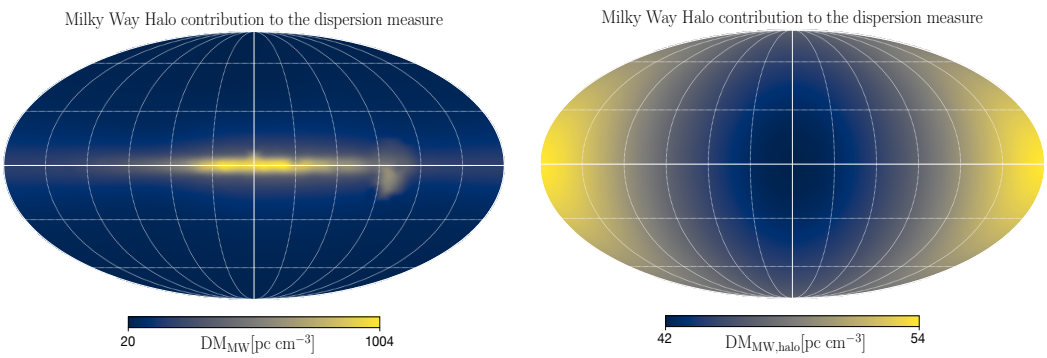

Figure 2: *Left*: Contribution of the MW to the DM, calculated using the code from Ocker and Cordes (2024). *Right*: Possible contribution to the DM from the MW halo, shown in galactic coordinates. The profile is derived using the model presented in Reischke et al. (2025) for a halo $M = 1.5 \times 10^{12} M_\odot$.

hydrodynamic simulations (Jaroszyński, 2020; Medlock et al., 2024; Theis et al., 2024). There is no agreement on whether there is a functional form to describe the probability distribution function of the host. However, a log-normal distribution can describe current data sufficiently well. In Figure 1, we show the typical form of the host contribution as found in simulation and its dependence on mass.

2.1.2 The Milky Way contribution

The distinction of the MW contribution is useful because $\mathrm{DM_{MW}}$ can be modeled quite accurately at high galactic latitudes (Yao et al., 2017; Ocker et al., 2020; Reischke and Hagstotz, 2023) using pulsar DMs. $\mathrm{DM_{MW,halo}}$, however, is less well constrained and can vary significantly (e.g. Prochaska and Zheng, 2019; Yamasaki and Totani, 2020; Cook et al., 2023), with values reaching up to $100\,\mathrm{pc\,cm^{-3}}$, these are, though, still debated. To first order, one can of course model this contribution by a spherically symmetric halo (see e.g. Keating and Pen, 2020). In Figure 2 we show the contribution of the MW and the MW halo. For the former we use the model by Ocker and Cordes (2024) and the MW halo contribution is calculated with the model described in Reischke et al. (2025).

One can see that at low galactic latitude the disk dominates and therefore produces large DM. For $l > 30$, however, the halo contribution can become more important. Understanding both contributions will become very important to unlocking FRB science. Here, the SKA can deliver a unique view into the southern hemisphere.

2.1.3 The cosmological contribution

$\mathrm{DM_{cosmic}}$ inherits the statistical properties of the LSS. Using Eq. (1), one can express it as follows:

$$\mathrm{DM_{cosmic}}(\boldsymbol{x}, z) = \frac{3\Omega_{\rm b0}\chi_{\rm H}}{8\pi G m_{\rm p}}\chi_{\rm e}\int_0^z \frac{1+z'}{E(z')} f(z')\left[1+\delta_{\rm e}(\boldsymbol{x}, z')\right]\mathrm{d}z', \tag{3}$$

with the dimensionless baryon density parameter $\Omega_{\rm b0}$ today, the Hubble radius, $\chi_{\rm H} = c/H_0$, the proton mass $m_{\rm p}$, the number of electrons per baryon $\chi_{\rm e}$ and the gravitational constant G. $\delta_{\rm e}$ is the electron density contrast, $E(z)$ is the expansion function, and $f(z)$ is the fraction of ionised

baryons, as only these electrons contribute to the DM. The average of Eq. (3) yields the well-known Macquart relation (Macquart et al., 2020).

2.2 Scattering

Scattering arises due to the multi-path propagation of the burst through an ionized medium. Inhomogeneities in the electron density transverse to the line of sight lead to a frequency-dependent deflection in the rays:

$$\alpha = \frac{\lambda^2 r_e}{2\pi} \int \nabla_\perp n_e(\mathbf{x}, s)\, \mathrm{d}s, \tag{4}$$

where α is the bending angle, λ is the wavelength at the scatterer, and $\nabla_\perp$ refers to the gradient in the coordinate transverse to the line of sight, $\mathbf{x}$. When the bending angle is sufficiently large, multiple rays may connect the source to the observer, with offset times of arrival. While the term 'plasma lensing' describes this phenomenon more generally, the term 'scattering' is typically used to refer to situations where there are a large number of such rays and observable quantities are computed statistically. The primary observable is the scattering timescale, or the mean time delay of the deflected rays relative to the direct line of sight, $\tau_{\mathrm{scatt.}} = \frac{1+z}{2c}\frac{d_{\mathrm{sl}} d_{\mathrm{lo}}}{d_{\mathrm{so}}}\langle\alpha^2\rangle$, where d_{sl}, d_{lo}, and d_{so} are the (angular diameter) distances between the source and scatterer, scatterer and observer, and source and observer, respectively. When the scattering time is large relative to the intrinsic burst width, scattering manifests as an exponential 'scattering tail' in the burst with a frequency-dependent width. The width of this tail is measured to determine the scattering time. When the scattering time is small relative to the intrinsic burst width, the images interfere at the observer, leading to a frequency-dependent scintillation pattern. The 'scintillation bandwidth' is measured and is related to the scattering time via $\Delta\nu_{\mathrm{scint}} = 2\pi/\tau_{\mathrm{scatt.}}$ (Pradeep E. T. et al., 2025).

The frequency dependence of these quantities can be used to confirm the scattering origin of the observed effect, with $\tau_{\mathrm{scatt.}} \propto \nu^{-\delta}$, where $\delta \sim [4, 4.4]$. The scaling $\delta = 4$ arises when the scattering is purely geometric (for which Eq. 4 holds) and $\delta = 4.4$ when the scattering is purely diffractive (i.e. wave optics hold) and the medium is Kolmogorov turbulent (Ocker et al., 2025). Common sites of scattering include the Milky Way and host ISM, manifesting as interstellar scintillation. Multi-screen scintillation measurements suggest that the ubiquitous scattering tails observed in FRBs may originate near the source, potentially in the circumburst environment Ocker et al. (2022b); Sammons et al. (2023). Scattering from the circumgalactic medium of intervening halos has yet to be definitively detected (see Faber et al. (2024) for a tentative detection), but scattering from the CGM could shed light on sub-grid physics in the CGM (see Caleb et al., 2026).

2.3 Rotation Measure

The linearly polarised synchrotron emission from FRBs undergoes Faraday rotation due to free electrons and magnetic fields parallel to the line-of-sight, $B_\parallel$. Faraday rotation leads to the rotation of the polarisation plane as a function of the observing wavelength, λ, as $\Delta\psi = \mathrm{RM}\,\lambda^2$, where $\Delta\psi$ is the change in the polarisation angle between the source and observer and RM is the rotation measure, given by

$$\mathrm{RM} = \frac{1}{2\pi}\frac{e^3}{m_e^2 c^4} \int_0^{d_{\mathrm{FRB}}} n_{\mathrm{e}}\, B_\parallel\, \mathrm{d}l\,, \tag{5}$$

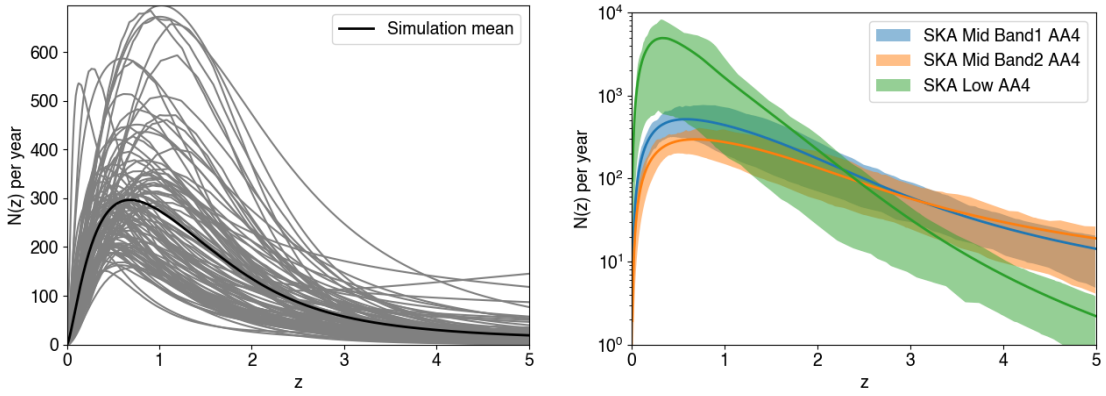

Figure 3: Predicted redshift distribution of FRBs detected by SKA. Left: predictions for band 2 of SKA Mid in AA4 configuration. The grey lines represent 100 instances of parameter sets fit to current FRB data; the black line represents the mean of these predictions. Right: predictions for different SKA observations, showing the means (lines), and 16–84% quantiles (shaded). Normalisation is such that the total rate in a full year's worth of observation time is given by $\int N(z)\,\mathrm{d}z$.

where e and m_e are the electron charge and mass, respectively. Like Equation (2), the RM of an FRB can also be expressed as a sum of different contributions,

$$\mathrm{RM_{obs}}(\mathbf{x}, z) = \mathrm{RM_{host}}(z) + \mathrm{RM_{cosmic}}(\mathbf{x}, z) + \mathrm{RM_{MW,ISM}}(\mathbf{x}) + \mathrm{RM_{MW,CGM}}(\mathbf{x}) + \mathrm{RM_{noise}}(\mathbf{x}), \quad (6)$$

where $\mathrm{RM_{host}}$ is the host contribution (including both the local environment and the host galaxy), $\mathrm{RM_{cosmic}}$ is the contribution to magnetised plasma in the intergalactic medium and the large-scale structure, $\mathrm{RM_{MW,ISM}}$ is from the Galactic ISM, $\mathrm{RM_{MW,CGM}}$ is from the Milky Way's CGM, and $\mathrm{RM_{noise}}$ quantifies the level of the fluctuations due to instrumental effects and analysis methods. Knowing n_e from DM contributions, RM could be used to infer the properties of galactic and intergalactic magnetic fields.

3 Expected data with SKA

In this section, we provide forecasts for the number of FRBs to be detected with SKA-mid and SKA-low for both AA* and AA4. The numbers presented here serve as the basis for the cosmological forecasts in the FRB chapters.

Table 1: Parameters used to model the FRB detection rate of SKA telescopes: mean frequency $\bar{\nu}$, bandwidth $\Delta\nu$, channel width $\delta\nu$, time resolution t_res, field of view (FOV), detection thresholds F_th for AA4 and AA*.

Instrument	$\bar{\nu}$	$\Delta\nu$	$\delta\nu$	t_res	FOV	$F_\mathrm{th}^\mathrm{AA4}$	$F_\mathrm{th}^\mathrm{AA^*}$
	MHz	MHz	MHz	ms	deg^2	Jy ms	Jy ms
Mid Band 2	1400	300	0.1075	0.069	0.58	0.059	0.116
Mid Band 1	865	300	0.1075	0.069	1.79	0.091	0.167
Low	190	120	0.0145	0.069	5.12	0.143	0.164

3.1 Simulating SKA detection of FRBs

Calculations of the number of FRBs detected by SKA telescopes, and their redshift–dispersion measure distribution, require three ingredients: properties of the detecting instrument, a treatment of the intrinsic FRB population, and a model for the cosmological distribution of ionised gas. Relevant properties of the former are given in Table 1, corresponding to tied beams from the central stations being used to cover the FOV out to the half-power point. We do not include a detailed model of the tied-beam shape and assume a Gaussian primary beam. The FRB population is modelled with a Schechter luminosity function characterised by power-law slope γ and turnover energy $E_{\rm max}$, a spectral index α, and source evolution scaling with the star-formation rate modelled by Madau and Dickinson (2014) as $\mathrm{SFR}(z)^n_{\rm sfr}$. Secondary parameters include the distribution of intrinsic FRB widths and scattering, which are taken from the fits of CHIME/FRB Collaboration et al. (2021b) —- no redshift dependence of this has yet been included, since the fit was to observed (and not rest-frame) properties; however, scattering is assumed to scale as ν^{-4}, and will be much more critical for SKA-Low. These parameters have been estimated based on FRB data from ASKAP, Parkes, FAST, and DSA by Hoffmann et al. (2025) using the `z-DM` code[2]. However, there are considerable uncertainties, so we iterate over 100 possible parameter sets chosen from the MCMC simulation of that work to illustrate the impact of these uncertainties on the forecasts. For the cosmological DM budget, we assume a Milky Way contribution from both the ISM and halo of $80\,\mathrm{pc\,cm^{-3}}$, a log-normal distribution of FRB host dispersion measures with parameters encoded in the MCMC data of Hoffmann et al. (2025), and cosmological contributions with mean, and fluctuations about the mean, described by Macquart et al. (2020).

These three sets of ingredients are combined in the simulation `z-DM`, which produces estimates for the FRB distribution in terms of redshift, extragalactic dispersion measure, and FRB luminosity. Figure 3 illustrates the expected redshift distribution in the case of SKA Mid band 2 in AA4 configuration — the variance due to parameter uncertainties is approximately a factor of 2. However, this variance increases significantly for SKA-low, since much less is known about the behaviour of FRBs at low frequencies. Table 2 lists the estimated annual rates.

For these estimates it was implicitly assumed that an FRB survey is operating commenusally with all SKA observations. In practice, the actual number of FRBs detected will depend on the relative fraction of the time observed in the different frequency bands of SKA-mid, as well as the sky position. The sample of FRBs predicted here are unique sources; dedicated follow-up of active repeaters may yield significantly higher numbers, which is not included in these estimates. Also, given the extremely uncertain detection rates at higher frequencies, we do not simulate estimates for SKA-mid bands 5a and 5b. Finally, these forecasts predict FRBs with DM $\lesssim 5000$ pc cm^{-3} will be discovered with SKA-mid, which is larger than the currently planned maximum searched DM = 3000 pc cm^{-3}. Given that the specifics of the SKA search pipeline are still in-progress and searches at high DMs have low computational cost, we make no cut in FRB DM in the following analyses.

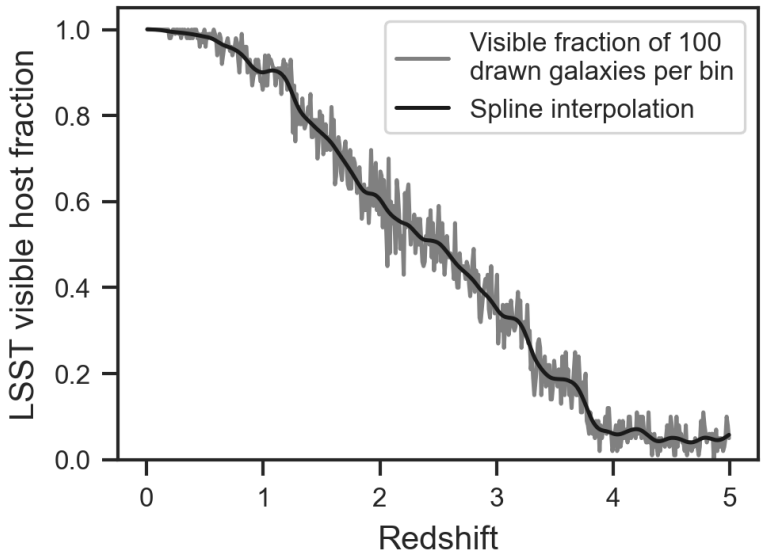

Figure 4: Fraction of FRB host galaxies that will be detected in one or more bands of the Rubin Observatory.

Table 2: Forecasted numbers of FRBs in one year of SKA on-sky observing and the fraction visible in the LSST. Reported numbers are the median, and the 16% and 84% quantiles.

Stage	Band	Nr. FRBs	Nr. visible hosts	Host fraction
AA*	Mid Band2	280^{+120}_{-110}	220^{+100}_{-80}	$0.79^{+0.05}_{-0.05}$
	Mid Band1	390^{+270}_{-140}	320^{+210}_{-110}	$0.83^{+0.04}_{-0.04}$
	Low	1320^{+5020}_{-750}	1230^{+4800}_{-700}	$0.94^{+0.02}_{-0.02}$
AA4	Mid Band2	550^{+270}_{-210}	420^{+200}_{-160}	$0.75^{+0.05}_{-0.05}$
	Mid Band1	790^{+530}_{-290}	620^{+440}_{-220}	$0.79^{+0.05}_{-0.04}$
	Low	1490^{+5700}_{-860}	1380^{+5420}_{-790}	$0.93^{+0.02}_{-0.03}$

3.2 Host visibility

The expected rate of FRB detections allows only for dedicated optical follow-up of a small fraction of the detections. Therefore, host identifications have to rely primarily on existing catalogues. Luckily, the SKA will show great synergy with the Rubin Observatory Legacy Survey of Space and Time (LSST, Ivezić et al., 2019).

We estimate the fraction of hosts that will be visible over the full 10 years of LSST, following Jahns-Schindler et al. (2023). We draw galaxies from their catalogue of galaxies simulated with the semi-analytic model of galaxy formation GALFORM (Cole et al., 2000; Baugh et al., 2019). For each of the 500 redshift bins used in the FRB forecast, we draw 100 galaxies weighted by their star formation rate. The simulated data include the observer frame brightness in each of the six Rubin Observatory bands. For a galaxy to be visible, we require the brightness in at least one of the

[2] https://github.com/FRBs/zdm

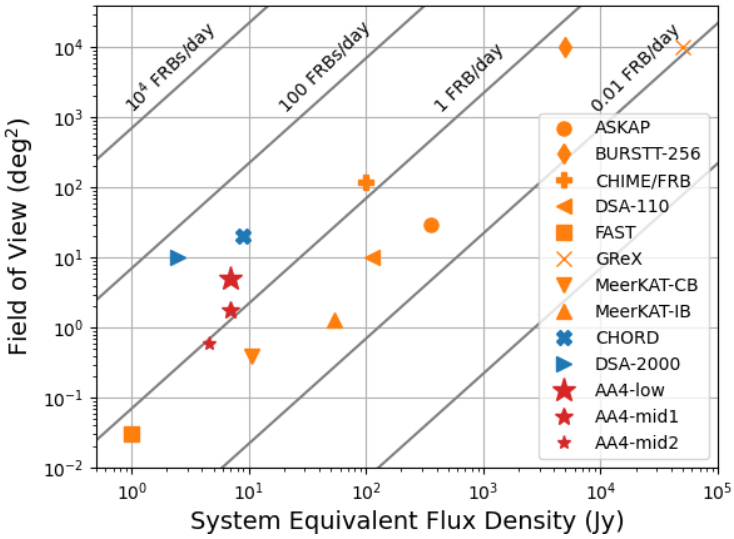

Figure 5: FRB detection rate parameter space plot. Current FRB surveys are shown in orange, upcoming surveys in blue, and the three SKA AA4 configurations and frequency bands discussed in the text in red. Based on the figure from Lin et al. (2022).

bands to exceed the target coadded 5-sigma depth after 10 years (Bianco et al., 2022). To apply the fractions to the previously simulated FRB numbers, we multiply each bin's observed fraction by its simulated FRB count and sum the products.

Figure 4 shows the redshift-dependent fraction. The resulting numbers of observed FRB host galaxies are presented in Table 2. The fraction is promising, spanning 0.75-0.94, although it becomes small above $z \sim 3$. It will likely be challenging to associate many galaxies with certainty above $z \sim 2$ because of the high probability of an unseen host.

3.3 FRB Survey Landscape

Advances in observational capabilities happen rapidly in the FRB field, and here we briefly discuss the future FRB survey landscape. Currently, two new telescopes with FRB science as one of the primary drivers are under construction. The Canadian Hydrogen Observatory and Radio-Transient Detector (CHORD) is being built in North America with the main telescope at the same site as CHIME/FRB and two outrigger stations with >1000 km baselines providing precise localisations (Vanderlinde et al., 2019). Its sensitivity is comparable to that of SKA-AA4 configurations, but it has an instantaneous field of view that is a factor of ~10 times larger (see Figure 5). As a result, its detection rate is an order of magnitude larger than SKA-mid. CHORD will be equipped with receivers with a continuous bandwidth from 300–1500 MHz, spanning most of the gap between SKA-low and SKA-mid band1, and extending into most of SKA-mid band 2.

The Deep Synoptic Array (DSA)-2000 is an array of small dishes to be constructed in Nevada, USA (Hallinan et al., 2019). It has high sensitivity and a moderate field of view, yielding a detection rate almost two orders of magnitude higher than that of SKA-mid AA4 configurations (Figure 5). The

operating range of the receivers is 0.7−2 GHz, which overlaps entirely with both SKA-mid bands and goes a few hundred MHz beyond in both directions.

Both CHORD and DSA-2000 are scheduled to begin operation around 2027. At the time of writing, the start of coordinated or long-term projects with the AA* configuration is expected in 2032 and 2034 for SKA-low and SKA-mid, respectively. Moreover, CHORD and DSA-2000 expect to detect ∼10,000 FRBs per year and have instantaneous bandwidths larger than those of SKA-mid band 1 and band 2 combined. Therefore, by the time AA* comes online, CHORD and DSA-2000 will likely have been operating for several years and have potentially discovered 10^5 FRBs.

The SKA, CHORD, and DSA-2000 are all narrow but deep surveys. In recent years, interest in wide but shallow surveys has been growing. These telescopes are aperture arrays of low-cost antennas that generally operate just below ∼1 GHz. BURSTT-256 is an example that is currently operational in Taiwan (Lin et al., 2022), but several additional arrays are under development worldwide. In the near future, these telescopes cannot compete in the absolute number of discoveries, but they can fill a role, for example, in discovering a population of local Universe sources, including Galactic FRBs.

4 Magnetic Fields in the High-Redshift Universe

Magnetic fields are present and important in a variety of astrophysical systems but are often challenging to measure observationally beyond the local Universe (Klein and Fletcher, 2015; Shukurov and Subramanian, 2021). FRBs could be very useful for probing magnetic fields in the early Universe, especially in high-redshift galaxies and in the intergalactic medium (IGM).

The $\mathrm{DM_{cosmic}}$ and $\mathrm{RM_{cosmic}}$ terms in Equation (2) and Equation (6), respectively, include contributions from both intervening galaxies and the IGM (including cosmic filaments and voids). These terms can be further decomposed as

$$\mathrm{DM_{cosmic}} = \sum_{i=1}^{N_{\mathrm{ingal}}} \frac{\mathrm{DM}_i(\mathbf{x})}{(1+z_{\mathrm{ingal},i})} + \mathrm{DM_{IGM}}(\mathbf{x}, z), \tag{7}$$

$$\mathrm{RM_{cosmic}} = \sum_{i=1}^{N_{\mathrm{ingal}}} \frac{\mathrm{RM}_i(\mathbf{x})}{(1+z_{\mathrm{ingal},i})^2} + \mathrm{RM_{IGM}}(\mathbf{x}, z), \tag{8}$$

where DM_i and RM_i denote the contributions from the ith intervening galaxy at redshift $z_{\mathrm{ingal},i}$, with N_{ingal} being the total number of intervening galaxies along the line of sight. The terms $\mathrm{DM_{IGM}}$ and $\mathrm{RM_{IGM}}$ represent the contributions from the IGM.

Below, in Sec. 4.1 and Sec. 4.2, we discuss the significance of magnetic fields in high-redshift galaxies and in the IGM, along with possible approaches to study them with SKA.

4.1 Magnetic fields in high-redshift intervening galaxies

Magnetic fields in the early Universe are observed to be orders of magnitude weaker ($\approx 10^{-10}\,\mu$G, see Kulsrud et al., 1997; Subramanian, 2016; Seta and Federrath, 2020) than those in present-day galaxies ($\approx 10^{1}\,\mu$G, see Beck, 2015; Haverkorn, 2015; Seta and McClure-Griffiths, 2025). This amplification is believed to result from a dynamo process that converts the kinetic energy of

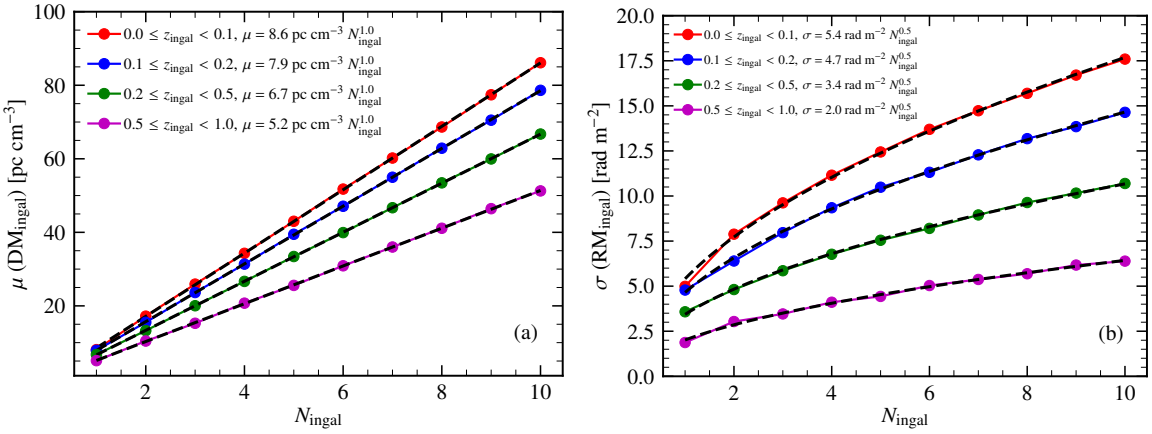

Figure 6: Mean and standard deviation of the dispersion and rotation measures from intervening galaxies, μ (DM$_{\rm ingal}$) (a) and σ (RM$_{\rm ingal}$) (b), for galaxies at different redshifts (see legend). These values are based on simple analytic models for the thermal electron density and magnetic fields (see text). Across all redshift bins, μ (DM$_{\rm ingal}$) $\propto N_{\rm ingal}{}^{1}$ and σ (RM$_{\rm ingal}$) $\propto N_{\rm ingal}{}^{0.5}$.

turbulence into magnetic energy (Ruzmaikin et al., 1988; Brandenburg and Subramanian, 2005; Rincon, 2019; Shukurov and Subramanian, 2021). Such amplification is seen in a variety of magnetohydrodynamic simulations (Schekochihin et al., 2004; Haugen et al., 2004; Gent et al., 2013; Seta et al., 2020; Seta and Federrath, 2021; Gent et al., 2023) but convincing observational evidence is still lacking. There have been some efforts in this direction using RM from radio galaxies, including both statistical studies (Bernet et al., 2008; Farnes et al., 2014; Malik et al., 2020; Shah and Seta, 2021; Amaral et al., 2021) and individual detections in gravitationally lensed systems (Mao et al., 2017; Kovacs et al., 2025). However, the statistical samples are highly inhomogeneous, and the lensed systems are biased toward more massive galaxies. Most importantly, both approaches require assumptions about the thermal electron density in order to extract magnetic field information from the observed RM, and these properties are highly uncertain. With DMs from FRBs, the magnetic field can be constrained more accurately, and with dense redshift sampling, its properties as a function of redshift can be mapped. Such an in-depth study would help constrain dynamo theories and improve galaxy evolution simulations.

Several previous studies have used cosmological simulations to investigate the RM and DM contributions from each component in Equation (2) and Equation (6) (Akahori et al., 2016; Hackstein et al., 2019, 2020; Kovacs et al., 2024), though some did not further decompose DM$_{\rm cosmic}$ and RM$_{\rm cosmic}$ as in Equation (7) and Equation (8). A recent investigation with the FLIMFLAM survey does indicate that the contribution of RM$_{\rm ingal}$ to the observed FRB RMs is non-negligible (Khrykin et al., 2026). We expect the total contributions of DM$_{\rm ingal}$ and RM$_{\rm ingal}$ to correlate with the number of intervening galaxies, $N_{\rm ingal}$. Once DM$_{\rm cosmic}$ and RM$_{\rm cosmic}$ are determined (already a challenge given the uncertainties in other terms in Equation (2) and Equation (6)), a fraction of them should correlate with $N_{\rm ingal}$ (such a correlation has been hinted at in DM observations, see Hussaini et al., 2025). Here, we estimate the dependence of DM$_{\rm ingal}$ and RM$_{\rm ingal}$ on $N_{\rm ingal}$. Quantifying this dependence would allow us to subtract the contributions of intervening galaxies and thereby isolate the IGM terms, providing a way to constrain magnetic fields in the IGM (see Sec. 4.2 for further

Table 3: RM uncertainties given the band for AA4 stage of SKA.

Band	Frequency Range [MHz]	RM uncertainty [rad m^{-2}]
SKA-Low	50–350	0.008
SKA-Mid, Band 1	350–1050	0.4
SKA-Mid, Band 2	950–1760	4

discussion).

It is also expected that FRB sightlines intersect primarily the CGM of intervening galaxies rather than their ISM, with typical impact parameters in the range 1–100 kpc. The connection between ISM and CGM dynamics, and therefore their magnetic fields, is an area of active research (Pakmor et al., 2020; van de Voort et al., 2021; Shah et al., 2025). Consequently, we adopt simple models for the thermal electron density and magnetic fields in the CGM with a typical size of 200 kpc to estimate how the total $\mathrm{DM_{ingal}}$ and $\mathrm{RM_{ingal}}$ depend on N_{ingal}. For the thermal electron density, we assume a spherically symmetric beta model (e.g. see Miller and Bregman, 2013), $n_{\mathrm{e}}(r) = 5 \times 10^{-4}\,\mathrm{cm^{-3}}\left(1 + (r/10\,\mathrm{kpc})^2\right)^{-3/4}$. For the magnetic field magnitude, we use an analytic model guided by radio polarisation observations of nearby galaxies at smaller radii and by cosmological simulations at larger radii (e.g. Fig. 8 in Shah and Seta, 2021). Further, for the magnetic field scale, based on the large-scale field in nearby galaxies (Beck, 2015; Seta and Federrath, 2024), we assume that the magnetic field may change sign (due to a random process) on a 1 kpc scale along the path length.

Figure 6 shows the mean of $\mathrm{DM_{ingal}}$ (a) and standard deviation of $\mathrm{RM_{ingal}}$ (b) as a function of N_{ingal} for various redshift bins of the intervening systems. We find that $\mu\ (\mathrm{DM_{ingal}}) \propto {N_{\mathrm{ingal}}}^{1}$ and $\sigma\ (\mathrm{RM_{ingal}}) \propto {N_{\mathrm{ingal}}}^{0.5}$ with the magnitude for both decreasing with increasing redshift. Searching for such trends in the FRB sample with known intervening galaxies along the line of sight will help isolate the contribution from intervening galaxies. We note that these magnitudes might also depend on the assumed thermal electron density and magnetic fields but the overall trend should be consistent with more complex models, such as cosmological simulations.

From the order-of-magnitude values in Figure 6, DM variations should be detectable given the DM uncertainty of $\lesssim 1\,\mathrm{pc\,cm^{-3}}$. In contrast, the minimum reliably measurable RM depends on the frequency coverage. Estimating these limits (see Brentjens and de Bruyn, 2005, and assuming a signal-to-noise ratio of 6) for the AA4 configuration of the SKA (see Table 3) shows that detecting the excess RM from intervening galaxies is feasible.

4.2 Magnetic fields in the intergalactic medium

The origin of magnetic fields in the Universe remains an open question. In particular, the physical origin of the seed fields, which are later amplified by dynamo mechanisms in turbulent astrophysical environments (as discussed in Sec. 4.1) is unknown. These seed fields could be either primordial or astrophysical in origin (Widrow et al., 2012; Durrer and Neronov, 2013; Subramanian, 2016). Primordial fields may have been generated in the early Universe during inflation or phase transitions, while astrophysical seed fields could arise from the Biermann battery mechanism, outflows from

the first stars and AGNs, or plasma instabilities. Thus, it is important to observationally probe magnetic fields in the IGM, especially in cosmic filaments and voids, where FRBs could be of use.

FRB sightlines without detectable intervening galaxies or clusters and/or cases where their contributions can be statistically accounted for in Equation (7) and Equation (8) are useful for probing magnetic fields in the IGM. This approach complements other FRB-based methods, such as scattering and scintillation, for studying IGM magnetism (Ravi et al., 2016; Padmanabhan and Loeb, 2023). The IGM contribution, however, is expected to be small ($\lesssim 1\,\mathrm{rad\,m^{-2}}$), so even with the large number of FRBs expected from the SKA, a statistical analysis with multiple such lines of sight will likely be required.

5 Expansion of the Universe

FRBs can be used as distance estimator and therefore can be used to test the expansion rate of the Universe. There are different methods to tackle this. Here we discuss two options: (*i*) using the Macquart relation and (*ii*) exploiting strongly lensed FRBs. A more quantitative presentation of the constraints on the Hubble constant based on the simulations presented here is given in the companion chapter Caleb et al. (2026).

5.1 The Macquart relation

Since host-identified FRBs provide both a redshift estimate and an independent distance measure (their DM), the DM-z relation offers a direct test of the background cosmology (see Eq. 3). In several papers, the possibility of using FRBs to measure the expansion history of the Universe has been explored in detail (e.g. Walters et al., 2018, 2019; Hagstotz et al., 2022). These studies show that, from a large sample of FRBs, it becomes possible to constrain cosmological parameters, such as the Hubble constant (H_0), matter density (Ω_m), and potentially even properties of dark energy, while marginalising over both the host and Milky Way contribution. This shows the FRB's potential to complement traditional methods such as supernovae and baryon acoustic oscillations. With the SKA, the number of available FRBs is expected to increase substantially. For the SKA numbers presented in Section 3, we can anticipate having independent constraints at the level of 1 % on those key cosmological parameters. As discussed in the introduction, other experiments will yield similar FRB detection rates, and achieving a further order-of-magnitude increase in sensitivity would require detecting 10^2 more FRBs than current experiments, which is unlikely in the near term. Nevertheless, the SKA will contribute two critical complementary advantages. First, it will detect FRBs at high redshifts, thereby allowing us to probe the Universe at earlier epochs. Second, the SKA is uniquely positioned as the only telescope covering extensive areas of the southern hemisphere at these redshifts. This broad sky coverage will ensure that the sightlines to potential FRB detections are less correlated than they would be if all observations were restricted to the northern hemisphere. As a result, the SKA's observations will offer greater statistical independence and provide much-needed robustness against systematic effects as the FRB sample size grows. In conclusion, while the SKA may not deliver fundamentally new constraints on the expansion history itself, it will undoubtedly serve as a vital robustness check in an era where systematic effects increasingly dominate cosmological measurements.

5.2 Lensed FRBs

The delay between multiple images of a strongly lensed source whose luminosity varies with time can be used to estimate the Hubble constant (H_0) and constrain additional cosmological parameters, a technique known as time-delay cosmography (Birrer et al., 2024). Variable background sources used in the past include AGNs and, more recently, supernovae (Grillo et al., 2024). With their short duration, FRBs represent ideal sources for time-delay cosmography (Li et al., 2018). Using FRBs, it could even become feasible to measure cosmological parameters without modeling the mass profile of the lens (Wucknitz et al., 2021), removing the largest source of uncertainty in current results (Millon et al., 2020). However, finding FRBs strongly lensed by galaxies (L-FRBs) is challenging due to the rarity of the phenomenon. In fact, their lensing optical depth is of the order of 10^{-3} – 10^{-4}, depending on the source distance (Yue et al., 2022). Thus, finding L-FRBs requires sensitive telescopes capable of discovering thousands of FRBs per year. This is in the range of upcoming facilities such as CHORD and DSA-2000. The discovery rates presented in Table 1 imply that SKA could also contribute to this endeavor, detecting an order of one L-FRB per year across all observing bands.

Although SKA-Low is expected to find many more FRBs, the effect of pulse broadening due to multipath propagation in the lens galaxy could negatively impact the discovery rate of L-FRBs at lower frequencies (Ocker et al., 2022a). The extent of this effect is difficult to estimate due to the unknown degree of turbulence in the plasma of lens galaxies. However, since most lenses are elliptical and impact parameters in the lens plane are usually large, pulse broadening is probably low for most L-FRBs. Additionally, it could be possible to increase the detection rates by lowering the threshold of FRB searches in the direction of sightlines with high lensing optical depth, such as clusters (Sammons et al., 2025).

A second challenge in using L-FRBs for time-delay cosmography comes from the necessity of detecting multiple images of the same source (Connor and Ravi, 2023). Given typical delays of days to weeks and the limited fields of view of sensitive telescopes, the chance of detecting both images coincidentally is low. Thus, it would be necessary to identify L-FRBs detected in FRB searches, then predict the arrival window of subsequent images with a model of the lens, and finally use multiple telescopes worldwide to observe the second image. Given that the second image is usually weaker, sensitive telescopes would facilitate this endeavor, and SKA could play a role in this regard whenever its field of view overlaps with FRB hunting machines such as DSA-2000.

6 Tests of dark matter

6.1 Dark matter in host galaxies

The host contribution to the DM essentially measures a combination of the gas densities and source distributions. It is, therefore, an excellent test bed for physical processes on the scales of galaxies and is sensitive to astrophysical processes. Physically, the statistical properties of the host contribution arise from the probability distribution function of FRBs in galaxies as well as the distribution of the hot gas. The exact mechanism responsible for FRBs is still under debate. In almost all cases, however, they are associated with stars and are hence chosen to follow the stellar density.

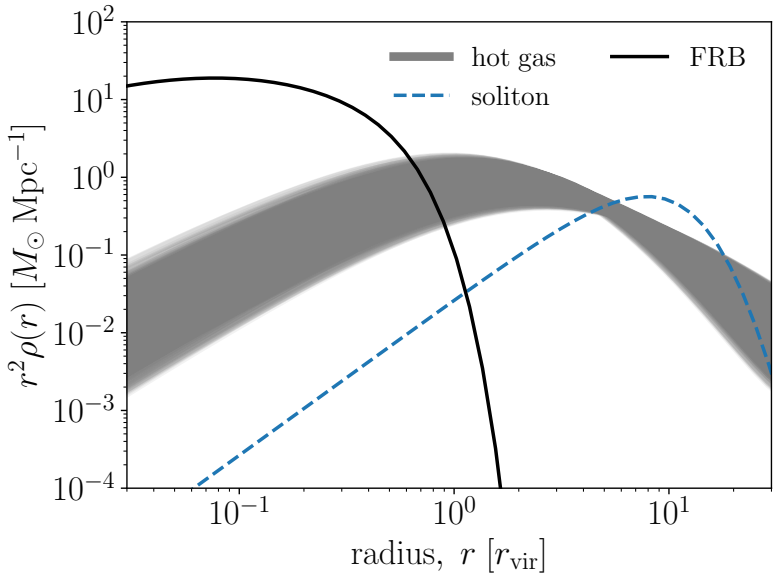

Figure 7: Normalised density profiles in an Milky Way-sized halo. Shown are stars (i.e. FRBs, solid black), the hot gas (free electrons, grey shaded area). The blue dashed profile shows a solitonic core of an axion-like particle of mass $m_{\mathrm{ALP}} = 10^{-23}$ eV.

Ultra-light dark matter such as axion-like particles (ALPs, see Marsh, 2016, for a review) form stable, localised field configurations. These configurations are known as solitons or axion mini-clusters. They may potentially alter the inner regions of density profiles observed in galactic halos. Physically, this effect can be interpreted as a quantum mechanical pressure. This arises due to the de Broglie wavelength of particles with very low mass. The wavelength can be on the scale of galaxies. As a result, the DM profile differs greatly from that of cold dark matter. These effects alter the underlying gas and stellar profiles in halos. The host contribution can therefore be used to measure the effect of ultra-light dark matter particles via their effect on the corresponding density profiles.

Example profiles are shown in Figure 7 for a Milky Way-like galaxy. The black line shows the distribution of stars, which indicates where FRBs will statistically originate from in the galaxy. In dashed blue the solitonic core of an ALP is shown. The grey area indicates the gas profile with uncertainties derived from (Kovač et al., 2025). While there exist no quantitative forecasts of this effect so far, the presence of ALPs will alter both the hot gas distribution, as well as the stellar density profile, and hence change the contribution expected from the host galaxy. In particular, pinpointing the FRB's position within the host itself, which will be possible at low redshift thanks to the SKAO's excellent resolution, may make it possible to statistically disentangle the different density profiles and put lower limits on the ALP mass as a lower ALP mass increases the effect and size of the solitonic core.

6.2 Microlensing

Microlensing by stellar-mass bodies produces multiple images of a background source. However, these micro-images are separated by orders of microseconds, too small to be resolved with current instruments. Thus, microlensing is at present only observed as a flux variation of the background source due to magnification. With FRBs, it could be possible to resolve, for the first time, micro-images in the time domain (Kader et al., 2022). In fact, the coherence of FRB signals is preserved by gravitational lensing, and thus, multiple micro-images can be identified in the autocorrelation of voltages measured by telescope antennas at the time of an FRB.

The detection of microlensing in the signal of FRBs has multiple applications, such as constraining the density of primordial black holes (Leung et al., 2022) and of MACHOs (Muñoz et al., 2016), identifying L-FRBs (Sathyanathan et al., 2025), assessing properties of lens galaxies (Meena and Saha, 2025), and even measuring cosmological parameters (Tsai et al., 2024). The SKA sensitivity will allow us to observe a large volume of the Universe. For example, the volume probed and its FRB discovery rate make SKA competitive in constraining the density of primordial black holes.

One potential show-stopper for gravitational microlensing is scattering. Identifying a gravitationally FRB relies on correlating the voltage signal between the two images, but if the images travel through different plasmas, multi-path propagation effects may alter their phases. Scattering can also affect magnification and time delays (Kumar and Beniamini, 2023). To avoid these effects, FRB surveys in the higher frequency bands, including SKA-mid bands 5a/5b are particularly powerful. We also note that need for voltage data for this science goal requires storing baseband data around detected FRBs.

7 Fundamental Physics

Effects from quantum gravity or other fundamental principles are usually complicated to detect using terrestrial experiments. Highly energetic astrophysical transients, however, are an excellent testbed for these effects due to the large distances covered, and hence the cumulative impact of intrinsically minor effects is lifted above the noise. The observed time delay, $\Delta t_{\rm obs}$, between frequency bands of an FRB comprises several contributions:

$$\Delta t_{\rm obs} = \Delta t_{\rm int} + \Delta t_{\rm LIV} + \Delta t_{\rm m} + \Delta t_{\rm grav}. \tag{9}$$

Here, $\Delta t_{\rm int}$ is an intrinsic delay, which includes the DM contribution $\Delta t_{\rm DM}$ and a possible source contribution $\Delta t_{\rm s}$. These delays are used in Equation (1) to infer the dispersion. However, the additional terms will lead to greater dispersion. The term $\Delta t_{\rm LIV}$ relates to Lorentz invariance violation (LIV), $\Delta t_{\rm m}$ could arise from dispersion if photons are massive, and $\Delta t_{\rm grav}$ is a (Shapiro) gravitational time delay. A lot of these tests can also be done with gamma-ray bursts. These are intrinsically more sensitive per object. However, FRBs are more abundant and measure these effects at a different energy scale.

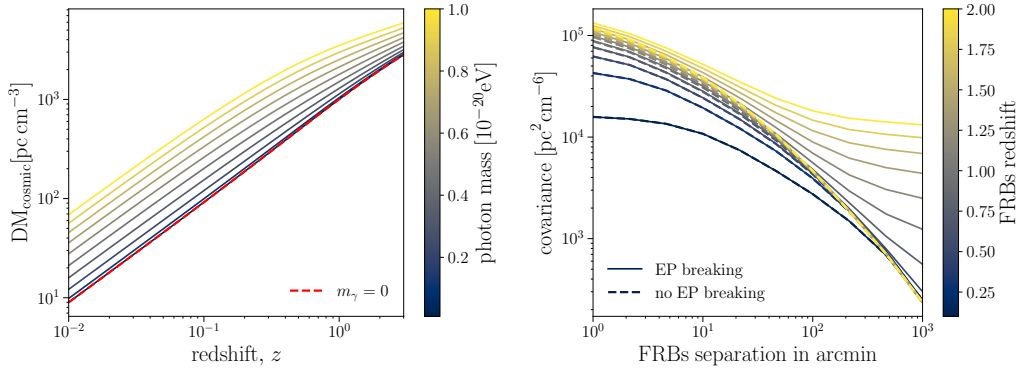

Figure 8: *Left*: The effect of massive photons on the cosmological DM, Equation (13). The dashed red line indicates the case where photons have vanishing mass, and the colourbar indicates the mass of the photons. *Right*: The covariance between different sightlines of FRBs as a function of their pairwise angular separation and the redshift of that pair as a colour scale. EP breaking is indicated as solid lines and the standard covariance as dashed lines.

7.1 Lorentz invariance

If Lorentz invariance is violated, the dispersion relation for photons can be expanded in the following model-independent form:

$$E^2 \simeq p^2c^2\left[1 - s_n\left(\frac{pc}{E_{\mathrm{LIV},n}}\right)^n\right], \tag{10}$$

where $E_{\mathrm{LIV},n}$ is the energy scale where LIV occurs expanded in n orders. s_n simply controls the sign of the LIV and whether these photons travel faster or slower than c. Calculating the group velocity allows us to infer the additional time delay (Jacob and Piran, 2008):

$$\Delta t_{\mathrm{LIV}} = s_n\frac{1+n}{2}\frac{E_1^n - E_2^n}{E_{\mathrm{LV},n}^n}\int_0^z \mathrm{d}z'\frac{(1+z')^n}{H(z')}, \tag{11}$$

here E_1 and E_2 are the upper and lower energies of the photons measured in the frequency band. Thus, decomposing the time delay into components with different frequency scalings allows separation of LIV terms, thereby constraining the amount of LIV at low photon energies.

7.2 Massive photons

Δt_{m} could arise from dispersion if photons are massive. This leads to a modified relativistic dispersion relation:

$$E^2 = c^2p^2 + m_\gamma^2c^4, \tag{12}$$

in turn resulting in an additional time delay (see e.g. Shao and Zhang, 2017)

$$\Delta t_{\mathrm{m}}(z) = \left(\frac{m_\gamma c^2}{4\pi\hbar}\right)^2\left(\nu_1^{-2} - \nu_2^{-2}\right)\int_0^z \frac{\mathrm{d}z'}{(1+z')^2H(z')}, \tag{13}$$

where ν_1^{-2} and ν_2^{-2} are the frequencies at which the time delay is measured. Due to the frequency dependence, this delay will contribute to the overall measured dispersion. Both Δt_{LIV} and Δt_{m}

Table 4: Expected uncertainties given the different stages and frequency bands of SKA for the mass of the photon, m_γ, and the equivalence principle breaking parameter, $\Delta\gamma$. Each combination of stage and band is given by to possible uncertainties, $\sigma_{\rm opt}$ and $\sigma_{\rm pess}$, corresponding to the best and the worst case from the simulated $N(z)$ in terms of number of FRBs (compare to Figure 3). All numbers are for a five years of observations.

		uncertainty as $[\sigma_{\rm opt},\sigma_{\rm pess}]$	
stage	band	$m_\gamma \times 10^{-23}$[eV]	$\Delta\gamma \times 10^{-14}$
AA*	SKA-Low	[0.28, 6.37]	[0.81, 14.3]
	SKA-Mid, Band 1	[1.26, 4.63]	[2.28, 9.82]
	SKA-Mid, Band 2	[1.51, 4.62]	[2.51, 10.7]
AA4	SKA-Low	[0.22, 5.67]	[0.63, 11.2]
	SKA-Mid, Band 1	[0.89, 3.31]	[1.83, 7.61]
	SKA-Mid, Band 2	[1.02, 3.42]	[2.78, 8.05]

cause non-zero effects on the cosmological background, acquiring additional DM. The left panel of Figure 8 shows the expected signal from $m_\gamma \neq 0$, showing that massive photons lead to an additional delay similar to $\mathrm{DM}_{\rm cosmic}$ but with a different redshift scaling due to the changed dispersion relation.

7.3 Equivalence principle

Since FRBs probe cosmological potentials, the standard Shapiro delay equation cannot be used due to its explicit gauge dependence and divergence (this is discussed in Minazzoli et al., 2019; Reischke et al., 2022; Reischke and Hagstotz, 2023). In a cosmological context, these issues can be mitigated by using a weakly perturbed Friedman-Robertson-Walker line element in the conformal Newtonian gauge within the parametrised post-Newtonian formalism framework:

$$\mathrm{d}s^2 = -\left(1+\frac{2\phi}{c^2}\right)c^2\mathrm{d}t^2 + a^2(t)\left(1-\frac{2\gamma\phi}{c^2}\right)\mathrm{d}\mathbf{x}^2\,, \tag{14}$$

where ϕ is the gauge potential, a the scale factor, and $\mathbf{x}$ the comoving coordinates. The time delay between photons of varying frequencies is given by

$$\Delta t_{\rm grav}(\hat{\boldsymbol{x}}) = \frac{\Delta\gamma}{c^3}\int_0^{\chi_{\rm s}} \mathrm{d}\chi\, a(\chi)\phi\big(\hat{\boldsymbol{x}}\chi, a(\chi)\big). \tag{15}$$

where χ represents the comoving distance at a background level. This formula does not diverge because it adheres to cosmological symmetry assumptions. Although it resembles the standard Shapiro delay equation, the perturbation ϕ acts as a random field with zero mean, allowing time delay to receive both positive and negative contributions along the line-of-sight (see also Bartlett et al., 2021, in the context of gamma ray bursts).

Any extra delay in arrival time between pulse frequencies can indicate a violation of the equivalence principle (EP)[3]. This extra dispersion is

$$\mathrm{DM}_{\rm obs}(\hat{\boldsymbol{x}}, z) \rightarrow \mathrm{DM}_{\rm obs}(\hat{\boldsymbol{x}}, z) + \mathrm{DM}_{\rm grav}(\hat{\boldsymbol{x}}, z). \tag{16}$$

[3]Our use of EP here refers to the weak equivalence principle.

$\mathrm{DM}_{\mathrm{grav}}(\hat{\boldsymbol{x}}, z)$ is the weak EP breaking term expressed as a DM along $\hat{\boldsymbol{x}}$ out to redshift z:

$$\mathrm{DM}_{\mathrm{grav}}(\hat{\boldsymbol{x}}, z) = \frac{\Delta\gamma}{\mathcal{K}c^3\left(\nu_1^{-2} - \nu_2^{-2}\right)} \int_0^{\chi(z)} \mathrm{d}\chi' a(\chi')\phi\big(\hat{\boldsymbol{x}}\chi', z(\chi')\big), \tag{17}$$

where $\mathcal{K} = e^2/(2\pi m_e c)$. Note that $\langle \mathrm{DM}_{\mathrm{grav}}(\hat{\boldsymbol{x}}, z)\rangle = 0$, i.e., on average there is no contribution to the mean dispersion (i.e., to the Macquart relation). However, one can use the scatter in the DM as a measure of the EP.

Reischke and Hagstotz (2023) calculated the covariance in the DM if the EP is broken. In Figure 8 on the right, the covariance is shown as a function of the angular separation between two FRB sight-lines with the FRBs at different redshifts. The EP breaking leads to large-scale correlations between different FRBs, since the additional dispersion is sensitive to potential fluctuations rather than density, introducing an additional k^{-2} factor via Poisson's equation. It is crucial to note that the mean DM-z relation is unaffected.

7.4 Forecast

In Table 4 we summarise the possible constraints on EP breaking as well as massive photons for the different stages and bands of SKA. Each single number corresponds to the 68 % confidence interval of the respective parameter. The given interval for each parameter corresponds to the most optimistic and pessimistic curve in terms of numbers of FRBs for each stage and band (compare Figures 3 and 6). We assume 5 years of operations for FRB observation and marginalise over the host and Milky Way contribution, assuming a prior on the cosmological parameters from Planck Collaboration et al. (2020). The forecast for the photon mass is a couple of magnitudes better than limits from Gamma-ray bursts (see e.g. Bartlett et al., 2021) thanks to the number of FRBs. Compared to the first constraints on the photon mass (see e,g, Bonetti et al., 2016), this is also a significant jump due to the larger redshifts of FRBs located and observed with SKA.

8 Conclusions

In this chapter we discuss the potential contributions of a population of FRBs discovered with the SKA to cosmology and fundamental physics. A companion chapter presents how the SKA-discovered FRBs can be used to study the distribution of baryons in the Universe: Caleb et al. (2026). Quantitative discussions were possible thanks to a distribution of FRBs over redshift generated using the population synthesis code `DM-z`. The fact that FRBs were discussed in chapters from several different SKA Science Working Groups demonstrates the broad interest in FRBs as cosmological probes.

We found that with a catalog of FRBs detected with the AA4 configuration, the magnetic fields in intervening galaxies (Section 4.1) could be measured. The SKA may detect ∼1 FRB per year that is lensed by a foreground galaxy or cluster. Such systems can be used, in principle, to measure cosmological parameters if the lensed images can also be detected, which will likely require dedicated follow-up by additional telescopes. The microlensing signature in FRBs can be used to constrain the density of, for example, primordial black holes or MACHOs, and due to the deliterious effects of scattering on the identification of FRB undergoing lensing, the highest bands

may give the SKA an advantage for this science case. In terms of fundamental physics, the catalog of SKA-discovered FRBs may provide a limit to the photon mass that is a few orders of magnitude better than what can be done with gamma-ray bursts.

In summary, the key strengths of the SKA are its sensitivity and frequency coverage. Sensitivity is critical for detecting sources out to large redshifts. While there are a few competing surveys coming online at similar frequencies as SKA-mid band 1 and band 2, we find that SKA-low will be peerless at its observing range and may find the majority of SKA-discovered FRBs. Given that propagation effects are highly frequency dependent, the low-frequency insight will be important for precise measurements of these effects in individual sources, as well as provide key insights into the systematics impacting statistical inference from large samples of FRBs.

Dedicated to the memory of J.P. Macquart, who wrote the original SKA FRB Science Book chapter "Fast Transients at Cosmological Distances with the SKA".

9 Acknowledgments

AS thanks Yik Ki (Jackie) Ma for several useful discussions. AS acknowledges support from the Australian Research Council's Discovery Early Career Researcher Award (DECRA, project DE250100003) and the Australia-Germany Joint Research Cooperation Scheme of Universities Australia (UA–DAAD, 2025–2026). LGS is a Lise Meitner Research Group leader and acknowledges funding from the Max Planck Society. D.M. acknowledges support from the French government under the France 2030 investment plan, as part of the Initiative d'Excellence d'Aix-Marseille Université – A*MIDEX (AMX-23-CEI-088). JJ-S acknowledges support through Australian Research Council Discovery Project DP220102305.

References

T. Akahori, D. Ryu, and B. M. Gaensler. *ApJ*, 824(2):105, June 2016. doi: 10.3847/0004-637X/824/2/105.

A. D. Amaral, T. Vernstrom, and B. M. Gaensler. *MNRAS*, 503(2):2913–2926, May 2021. doi: 10.1093/mnras/stab564.

D. J. Bartlett, H. Desmond, P. G. Ferreira, and J. Jasche. *PRD*, 104(10):103516, Nov. 2021. doi: 10.1103/PhysRevD.104.103516.

C. M. Baugh et al. *MNRAS*, 483(4):4922–4937, March 2019. doi: 10.1093/mnras/sty3427.

R. Beck. *A&A Rev.*, 24:4, Dec. 2015. doi: 10.1007/s00159-015-0084-4.

M. L. Bernet et al. *NAT*, 454(7202):302–304, July 2008. doi: 10.1038/nature07105.

F. B. Bianco et al. *ApJS*, 258(1):1, Jan. 2022. doi: 10.3847/1538-4365/ac3e72.

S. Birrer et al. *Space Sci. Rev.*, 220(5):48, Aug. 2024. doi: 10.1007/s11214-024-01079-w.

L. Bonetti et al. *Physics Letters B*, 757:548–552, June 2016. doi: 10.1016/j.physletb.2016.04.035.

A. Brandenburg and K. Subramanian. *Phys. Rep.*, 417(1-4):1–209, Oct. 2005. doi: 10.1016/j.physrep.2005.06.005.

M. A. Brentjens and A. G. de Bruyn. *A&A*, 441(3):1217–1228, Oct. 2005. doi: 10.1051/0004-6361:20052990.

M. Caleb et al. *MNRAS*, 524(2):2064–2077, 06 2023. ISSN 0035-8711. doi: 10.1093/mnras/stad1839. URL https://doi.org/10.1093/mnras/stad1839.

M. Caleb et al. *arXiv e-prints*, art. arXiv:2508.01648, Aug. 2025. doi: 10.48550/arXiv.2508.01648.

M. Caleb et al. In *Advancing Astrophysics with the SKA – II (AASKAII)*. 2026. arXiv search: Report number AASKAII/Caleb01.

CHIME Collaboration et al. *ApJS*, 261(2):29, Aug. 2022. doi: 10.3847/1538-4365/ac6fd9. URL https://ui.adsabs.harvard.edu/abs/2022ApJS..261...29C.

CHIME/FRB Collaboration et al. *ApJS*, 257(2):59, December 2021a. doi: 10.3847/1538-4365/ac33ab.

CHIME/FRB Collaboration et al. *ApJS*, 257(2):59, dec 2021b. doi: 10.3847/1538-4365/ac33ab. URL https://dx.doi.org/10.3847/1538-4365/ac33ab.

S. Cole, C. G. Lacey, C. M. Baugh, and C. S. Frenk. *MNRAS*, 319(1):168–204, November 2000. doi: 10.1046/j.1365-8711.2000.03879.x.

L. Connor and V. Ravi. *MNRAS*, 521(3):4024–4038, May 2023. doi: 10.1093/mnras/stad667.

A. M. Cook et al. *ApJ*, 946(2):58, Apr. 2023. doi: 10.3847/1538-4357/acbbd0.

A. P. Curtin et al. In *Advancing Astrophysics with the SKA – II (AASKAII)*. 2026. arXiv search: Report number AASKAII/Curtin01.

R. Durrer and A. Neronov. *A&A Rev.*, 21:62, June 2013. doi: 10.1007/s00159-013-0062-7.

J. T. Faber et al. *arXiv e-prints*, art. arXiv:2405.14182, May 2024. doi: 10.48550/arXiv.2405.14182.

J. S. Farnes, S. P. O'Sullivan, M. E. Corrigan, and B. M. Gaensler. *ApJ*, 795(1):63, Nov. 2014. doi: 10.1088/0004-637X/795/1/63.

F. A. Gent et al. *MNRAS*, 430:L40–L44, Mar. 2013. doi: 10.1093/mnrasl/sls042.

F. A. Gent, M.-M. Mac Low, M. J. Korpi-Lagg, and N. K. Singh. *ApJ*, 943(2):176, Feb. 2023. doi: 10.3847/1538-4357/acac20.

C. Grillo, L. Pagano, P. Rosati, and S. H. Suyu. *A&A*, 684:L23, Apr. 2024. doi: 10.1051/0004-6361/202449278.

S. Hackstein et al. *MNRAS*, 488(3):4220–4238, Sept. 2019. doi: 10.1093/mnras/stz2033.

S. Hackstein, M. Brüggen, F. Vazza, and L. F. S. Rodrigues. *MNRAS*, 498(4):4811–4829, Nov. 2020. doi: 10.1093/mnras/staa2572.

S. Hagstotz, R. Reischke, and R. Lilow. *MNRAS*, 511(1):662–667, Mar. 2022. doi: 10.1093/mnras/stac077.

G. Hallinan et al. In *BAAS*, volume 51, page 255, Sept. 2019. doi: 10.48550/arXiv.1907.07648.

N. E. Haugen, A. Brandenburg, and W. Dobler. *Phys. Rev. E*, 70(1):016308, July 2004. doi: 10.1103/PhysRevE.70.016308.

M. Haverkorn. In A. Lazarian, E. M. de Gouveia Dal Pino, and C. Melioli, editors, *Magnetic Fields in Diffuse Media*, volume 407 of *Ap&SS Library*, page 483, Jan. 2015. doi: 10.1007/978-3-662-44625-6_17.

J. L. Hoffmann et al. *PASA*, 42:e017, Jan. 2025. doi: 10.1017/pasa.2024.127.

A. W. Hotan et al. *PASA*, 38:e009, March 2021. doi: 10.1017/pasa.2021.1.

M. Hussaini et al. *arXiv e-prints*, art. arXiv:2506.04186, June 2025. doi: 10.48550/arXiv.2506.04186.

Ž. Ivezić et al. *ApJ*, 873(2):111, Mar. 2019. doi: 10.3847/1538-4357/ab042c.

U. Jacob and T. Piran. *J. Cosmology Astropart. Phys.*, 2008(1):031, Jan. 2008. doi: 10.1088/1475-7516/2008/01/031.

J. N. Jahns-Schindler, L. G. Spitler, C. R. H. Walker, and C. M. Baugh. *MNRAS*, 523(4):5006–5023, Aug. 2023. doi: 10.1093/mnras/stad1659. URL https://ui.adsabs.harvard.edu/abs/2023MNRAS.523.5006J.

M. Jaroszyński. *Acta Astron.*, 70(2):87–100, June 2020. doi: 10.32023/0001-5237/70.2.1.

Z. Kader et al. *PRD*, 106(4):043016, Aug. 2022. doi: 10.1103/PhysRevD.106.043016.

L. C. Keating and U.-L. Pen. *MNRAS*, 496(1):L106–L110, July 2020. doi: 10.1093/mnrasl/slaa095.

I. S. Khrykin et al. *A&A*, 706:A11, Jan. 2026. doi: 10.1051/0004-6361/202557213.

U. Klein and A. Fletcher. *Galactic and Intergalactic Magnetic Fields*. 2015.

T. O. Kovacs et al. *A&A*, 690:A47, Oct. 2024. doi: 10.1051/0004-6361/202347459.

T. O. Kovacs et al. *arXiv e-prints*, art. arXiv:2507.12542, July 2025. doi: 10.48550/arXiv.2507.12542.

M. Kovač et al. *J. Cosmology Astropart. Phys.*, 2025(11):046, Nov. 2025. doi: 10.1088/1475-7516/2025/11/046.

R. M. Kulsrud, R. Cen, J. P. Ostriker, and D. Ryu. *ApJ*, 480(2):481–491, May 1997. doi: 10.1086/303987.

P. Kumar and P. Beniamini. *MNRAS*, 520(1):247–258, Mar. 2023. doi: 10.1093/mnras/stad160.

C. J. Law et al. *arXiv e-prints*, art. arXiv:2307.03344, July 2023. doi: 10.48550/arXiv.2307.03344. URL https://ui.adsabs.harvard.edu/abs/2023arXiv230703344L.

C. Leung et al. *PRD*, 106(4):043017, Aug. 2022. doi: 10.1103/PhysRevD.106.043017.

Z.-X. Li et al. *Nature Communications*, 9:3833, Sept. 2018. doi: 10.1038/s41467-018-06303-0.

H.-H. Lin et al. *PASP*, 134(1039):094106, Sept. 2022. doi: 10.1088/1538-3873/ac8f71.

J. P. Macquart et al. *nat*, 581(7809):391–395, May 2020. doi: 10.1038/s41586-020-2300-2.

P. Madau and M. Dickinson. *ARA&A*, 52:415–486, Aug. 2014. doi: 10.1146/annurev-astro-081811-125615.

S. Malik, H. Chand, and T. R. Seshadri. *ApJ*, 890(2):132, Feb. 2020. doi: 10.3847/1538-4357/ab6bd5.

S. A. Mao et al. *Nature Astronomy*, 1:621–626, Aug. 2017. doi: 10.1038/s41550-017-0218-x.

D. J. E. Marsh. *Phys. Rep.*, 643:1–79, July 2016. doi: 10.1016/j.physrep.2016.06.005.

M. McQuinn. *ApJL*, 780:L33, Jan. 2014. ISSN 0004-637X. doi: 10.1088/2041-8205/780/2/L33. URL http://adsabs.harvard.edu/abs/2014ApJ...780L..33M.

I. Medlock et al. *ApJ*, 967(1):32, May 2024. doi: 10.3847/1538-4357/ad3070.

A. K. Meena and P. Saha. *arXiv e-prints*, art. arXiv:2507.20305, July 2025. doi: 10.48550/arXiv.2507.20305.

M. J. Miller and J. N. Bregman. *ApJ*, 770(2):118, June 2013. doi: 10.1088/0004-637X/770/2/118.

M. Millon et al. *A&A*, 639:A101, July 2020. doi: 10.1051/0004-6361/201937351.

O. Minazzoli, N. K. Johnson-McDaniel, and M. Sakellariadou. *PRD*, 100(10):104047, Nov. 2019. doi: 10.1103/PhysRevD.100.104047.

J. B. Muñoz, E. D. Kovetz, L. Dai, and M. Kamionkowski. *PRL*, 117(9):091301, Aug. 2016. doi: 10.1103/PhysRevLett.117.091301.

C.-H. Niu et al. *ApJL*, 909(1):L8, Mar. 2021. doi: 10.3847/2041-8213/abe7f0.

S. K. Ocker and J. M. Cordes. *Research Notes of the American Astronomical Society*, 8(1):17, Jan. 2024. doi: 10.3847/2515-5172/ad1bf1.

S. K. Ocker, J. M. Cordes, and S. Chatterjee. *ApJ*, 897(2):124, July 2020. doi: 10.3847/1538-4357/ab98f9.

S. K. Ocker, J. M. Cordes, S. Chatterjee, and M. R. Gorsuch. *ApJ*, 934(1):71, July 2022a. doi: 10.3847/1538-4357/ac75ba.

S. K. Ocker et al. *ApJ*, 931(2):87, June 2022b. doi: 10.3847/1538-4357/ac6504.

S. K. Ocker, M. C. Chen, S. P. Oh, and P. Sharma. *ApJ*, 988(1):69, July 2025. doi: 10.3847/1538-4357/ade0bc.

H. Padmanabhan and A. Loeb. *ApJL*, 946(1):L18, Mar. 2023. doi: 10.3847/2041-8213/acc3a1.

R. Pakmor et al. *MNRAS*, 498(3):3125–3137, Nov. 2020. doi: 10.1093/mnras/staa2530.

E. Petroff, J. W. T. Hessels, and D. R. Lorimer. *A&A Rev.*, 27(1):4, May 2019. doi: 10.1007/s00159-019-0116-6. URL https://ui.adsabs.harvard.edu/abs/2019A&ARv..27....4P.

Planck Collaboration et al. *A&A*, 641:A6, Sept. 2020. ISSN 0004-6361. doi: 10.1051/0004-6361/201833910. URL http://adsabs.harvard.edu/abs/2020A%26A...641A...6P.

S. Pradeep E. T. et al. *A&A*, 700:A99, Aug. 2025. doi: 10.1051/0004-6361/202554202.

J. X. Prochaska and Y. Zheng. *MNRAS*, 485(1):648–665, May 2019. doi: 10.1093/mnras/stz261.

K. M. Rajwade et al. *MNRAS*, 514(2):1961–1974, Aug. 2022. doi: 10.1093/mnras/stac1450.

V. Ravi et al. *Science*, 354(6317):1249–1252, Dec. 2016. doi: 10.1126/science.aaf6807.

R. Reischke and S. Hagstotz. *MNRAS*, 523(4):6264–6271, Aug. 2023. doi: 10.1093/mnras/stad1866.

R. Reischke, S. Hagstotz, and R. Lilow. *MNRAS*, 512(1):285–290, May 2022. doi: 10.1093/mnras/stab3571.

R. Reischke et al. *The Open Journal of Astrophysics*, 8:127, Sept. 2025. doi: 10.33232/001c.143819.

F. Rincon. *Journal of Plasma Physics*, 85(4):205850401, Aug. 2019. doi: 10.1017/S0022377819000539.

A. A. Ruzmaikin, D. D. Sokolov, and A. M. Shukurov. *Magnetic Fields of Galaxies*, volume 133. 1988. doi: 10.1007/978-94-009-2835-0.

M. W. Sammons et al. *MNRAS*, 525(4):5653–5668, Nov. 2023. doi: 10.1093/mnras/stad2631.

M. W. Sammons et al. *ApJ*, 987(2):139, July 2025. doi: 10.3847/1538-4357/addc71.

G. Sathyanathan, C. Leung, O. Wucknitz, and P. Saha. *arXiv e-prints*, art. arXiv:2504.10523, Apr. 2025. doi: 10.48550/arXiv.2504.10523.

A. A. Schekochihin et al. *ApJ*, 612(1):276–307, Sept. 2004. doi: 10.1086/422547.

A. Seta and C. Federrath. *MNRAS*, 499(2):2076–2086, Dec. 2020. doi: 10.1093/mnras/staa2978.

A. Seta and C. Federrath. *Physical Review Fluids*, 6(10):103701, Oct. 2021. doi: 10.1103/PhysRevFluids.6.103701.

A. Seta and C. Federrath. *MNRAS*, 533(2):1875–1886, Sept. 2024. doi: 10.1093/mnras/stae1935.

A. Seta and N. M. McClure-Griffiths. *MNRAS*, 539(2):1024–1039, May 2025. doi: 10.1093/mnras/staf520.

A. Seta, P. J. Bushby, A. Shukurov, and T. S. Wood. *Physical Review Fluids*, 5(4):043702, Apr. 2020. doi: 10.1103/PhysRevFluids.5.043702.

H. Shah and A. Seta. *MNRAS*, 508(1):1371–1388, Nov. 2021. doi: 10.1093/mnras/stab2500.

H. Shah, F. van de Voort, A. Seta, and C. Federrath. *MNRAS*, 541(3):2471–2492, Aug. 2025. doi: 10.1093/mnras/staf1066.

R. M. Shannon et al. *arXiv e-prints*, art. arXiv:2408.02083, Aug. 2024. doi: 10.48550/arXiv.2408.02083. URL https://ui.adsabs.harvard.edu/abs/2024arXiv240802083S.

L. Shao and B. Zhang. *PRD*, 95(12):123010, June 2017. doi: 10.1103/PhysRevD.95.123010.

A. M. Shukurov and K. Subramanian. *Astrophysical Magnetic Fields: From Galaxies to the Early Universe*. 2021. doi: 10.1017/9781139046657.

K. Subramanian. *Reports on Progress in Physics*, 79(7):076901, July 2016. doi: 10.1088/0034-4885/79/7/076901.

A. Theis, S. Hagstotz, R. Reischke, and J. Weller. *arXiv e-prints*, art. arXiv:2403.08611, Mar. 2024. doi: 10.48550/arXiv.2403.08611.

A. Tsai, D. L. Jow, D. Baker, and U.-L. Pen. *PRD*, 110(4):043503, Aug. 2024. doi: 10.1103/PhysRevD.110.043503.

F. van de Voort et al. *MNRAS*, 501(4):4888–4902, Mar. 2021. doi: 10.1093/mnras/staa3938.

K. Vanderlinde et al. In *Canadian Long Range Plan for Astronomy and Astrophysics White Papers*, volume 2020, page 28, Oct. 2019. doi: 10.5281/zenodo.3765414.

A. Walters et al. *ApJ*, 856(1):65, Mar. 2018. doi: 10.3847/1538-4357/aaaf6b.

A. Walters, Y.-Z. Ma, J. Sievers, and A. Weltman. *PRD*, 100(10):103519, Nov. 2019. doi: 10.1103/PhysRevD.100.103519.

L. M. Widrow et al. *Space Sci. Rev.*, 166(1-4):37–70, May 2012. doi: 10.1007/s11214-011-9833-5.

O. Wucknitz, L. G. Spitler, and U.-L. Pen. *A&A*, 645:A44, Jan. 2021. doi: 10.1051/0004-6361/202038248.

S. Yamasaki and T. Totani. *ApJ*, 888(2):105, Jan. 2020. doi: 10.3847/1538-4357/ab58c4.

J. M. Yao, R. N. Manchester, and N. Wang. *ApJ*, 835(1):29, Jan. 2017. doi: 10.3847/1538-4357/835/1/29.

M. Yue, X. Fan, J. Yang, and F. Wang. *ApJ*, 925(2):169, Feb. 2022. doi: 10.3847/1538-4357/ac409b.